Pure Appl. Geophys.

DOI 10.1007/s00024-011-0403-2

Pure and Applied Geophysics

A Quantitative Assessment of DInSAR Measurements of Interseismic Deformation: The Southern San Andreas Fault Case Study

Mariarosaria Manzo,[1] Yuri Fialko,[2] Francesco Casu,[1] Antonio Pepe,[1] and Riccardo Lanari[1]

Abstract—We investigate the capabilities and limitations of the Differential Interferometric Synthetic Aperture Radar (DInSAR) techniques, in particular of the Small BAseline Subset (SBAS) approach, to measure surface deformation in active seismogenetic areas. The DInSAR analysis of low-amplitude, long-wavelength deformation, such as that due to interseismic strain accumulation, is limited by intrinsic trade-offs between deformation signals and orbital uncertainties of SAR platforms in their contributions to the interferometric phases, the latter being typically well approximated by phase ramps. Such trade-offs can be substantially reduced by employing auxiliary measurements of the long-wavelength velocity field. We use continuous Global Positioning System (GPS) measurements from a properly distributed set of stations to perform a pre-filtering operation of the available DInSAR interferograms. In particular, the GPS measurements are used to estimate the secular velocity signal, approximated by a spatial ramp within the azimuth-range radar imaging plane; the phase ramps derived from the GPS data are then subtracted from the available set of DInSAR interferograms. This pre-filtering step allows us to compensate for the major component of the long-wavelength range change that, within the SBAS procedure, might be wrongly interpreted and filtered out as orbital phase ramps. With this correction, the final results are obtained by simply adding the pre-filtered long-wavelength deformation signal to the SBAS retrieved time series. The proposed approach has been applied to a set of ERS-1/2 SAR data acquired during the 1992–2006 time interval over a 200 × 200 km area around the Coachella Valley section of the San Andreas Fault in Southern California, USA. We present results of the comparison between the SBAS and the Line Of Sight (LOS)—projected GPS time series of the USGC/PBO network, as well as the mean LOS velocity fields derived using SBAS, GPS and stacking techniques. Our analysis demonstrates the effectiveness of the presented approach and provides a quantitative assessment of the accuracy of DInSAR measurements of interseismic deformation in a tectonically active area.

Key words: Deformation time series, differential SAR interferometry, Small BAseline Subset (SBAS), interseismic deformation, San Andreas Fault.

1. Introduction

Differential Synthetic Aperture Radar Interferometry (DInSAR) is a microwave remote sensing technique that allows measuring surface deformation with a centimeter to millimeter accuracy at high resolution (tens of meters) and large spatial coverage (Gabriel *et al.*, 1989). The DInSAR technique exploits the phase difference (interferogram) between two temporally separated SAR acquisitions to provide a measure of the ground deformation along the radar Line Of Sight (LOS).

Initially applied to characterize sizeable deformation events (Massonnet *et al.*, 1993, 1995; Peltzer and Rosen, 1995; Rignot, 1998; Amelung *et al.*, 1999; Fialko *et al.*, 2001), the DInSAR methodology has successively been adapted to analyze the temporal evolution of surface deformation via the generation of LOS displacement time series. For this purpose, the information available from each interferometric SAR data pair must be properly related to that contained in other pairs by generating and inverting an appropriate sequence of DInSAR interferograms. In this context, several advanced DInSAR approaches have been implemented; they can be grouped into two main categories: the Persistent Scatterer (PS) (Ferretti *et al.*, 2000; Werner *et al.*, 2003; Hooper *et al.*, 2004) and the Small Baseline (SB) (Berardino *et al.*, 2002; Mora *et al.*, 2003; Prati *et al.*, 2010) methods, although a solution that incorporates both the PS and SB approaches has also been recently proposed (Hooper, 2008). The first

[1] Istituto per il Rilevamento Elettromagnetico dell'Ambiente (IREA), National Council of Research (CNR), Via Diocleziano 328, 80124 Naples, Italy. E-mail: manzo.mr@irea.cnr.it

[2] Institute of Geophysics and Planetary Physics, Scripps Institution of Oceanography, University of California San Diego, La Jolla, CA 92093-0225, USA.

Published online: 30 September 2011

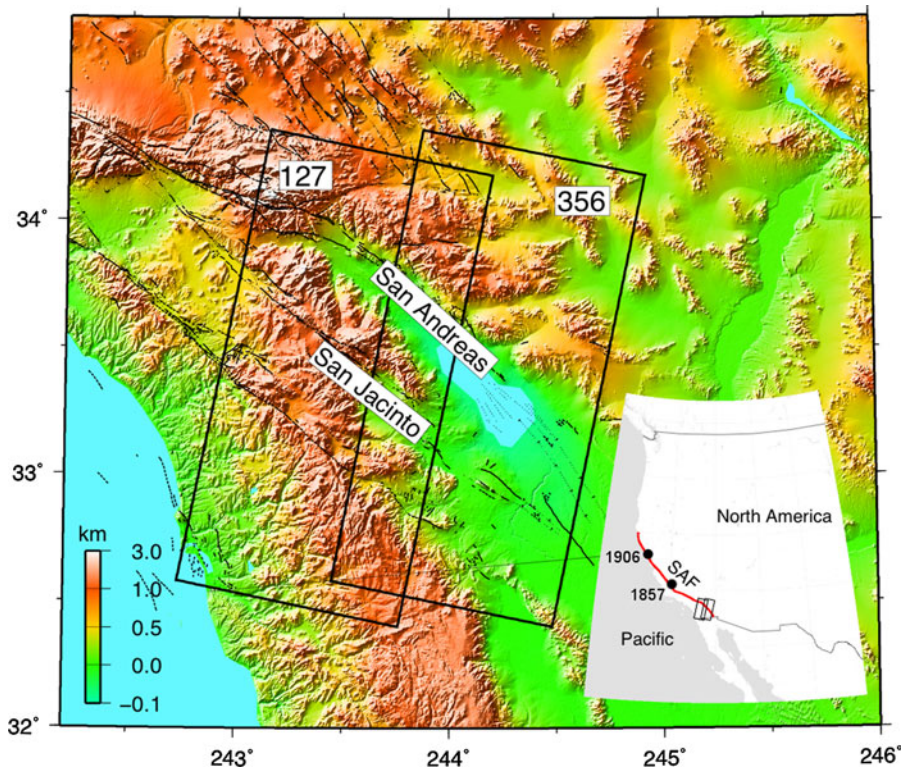

Figure 1
Shaded topography map of the study area. *Black wavy lines* denote active faults. *Black rectangles* represent ERS SAR tracks used in this study. The *red line* in the inset denotes the San Andreas Fault (SAF); moreover, the *black circles* indicate the locations of the 1857 and 1906 earthquakes

class of time-dependent DInSAR algorithms operates on single-look interferograms generated with respect to a selected common SAR image (usually referred to as "master image"), with no constraint on the spatial and temporal separation (baselines) of the SAR data pairs. The second approach considers a combination of SAR interferograms generated from an appropriate selection of the SAR data pairs characterized by relatively small baselines. In the latter case, both multi-look (Berardino *et al.*, 2002) and single-look (Lanari *et al.*, 2004a) interferograms can be analyzed. In this paper, we focus on the advanced SB-DInSAR technique referred to as Small BAseline Subset (SBAS) (Berardino *et al.*, 2002) approach that has previously been demonstrated to measure LOS velocities and displacements with an accuracy of about 1–2 mm/year and 5–10 mm, respectively (Lanari *et al.*, 2004b; Casu *et al.*, 2006; Manzo *et al.*, 2006; Lanari *et al.*, 2007a, b; Tizzani *et al.*, 2007; Neri *et al.*, 2009).

Deformation monitoring of seismogenetic areas is a key application of the DInSAR techniques, including both secular and transient deformation. However, in this case the presence of phase signal components within the generated differential interferograms, caused by inaccuracies in the SAR sensor orbit information, represents a key limitation. Orbital errors are typically well approximated by long-wavelength trends in the radar interferograms (Rosen *et al.*, 2000), usually referred to as orbital ramps. Distinguishing between deformation signals and phase patterns due to orbital uncertainties is critical for characterizing surface motions that result from interseismic deformation due to active faults. On the other hand, the estimation and subsequent removal of possible orbital phase artifacts remains a mandatory

operation that, if neglected, can lead to significant errors in the estimate of the inter-seismic strain accumulation (Peltzer *et al.*, 2001; Wright *et al.*, 2004; Fialko, 2006; Biggs *et al.*, 2007) and the retrieved deformation time series (Burgmann *et al.*, 2006; Gourmelen *et al.*, 2010).

One way to mitigate this problem is to exploit independent data. For instance, measurements from the continuous Global Positioning System (GPS) stations in the study area can provide important information about the long-wavelength spatial characteristics as well as the time dependence of the surface velocity field (e.g., Burgmann *et al.*, 2006). Although the spatial distribution of continuous GPS is typically limited compared to the one provided by the DInSAR technology, GPS measurements may be readily used to estimate and subsequently remove possible orbital phase artifacts (Fialko *et al.*, 2006; Gourmelen *et al.*, 2010). The DInSAR approach exploited below is rather simple because it has minimum impact on the SBAS processing chain; indeed, it is based on carrying out a pre-filtering operation of the available DInSAR interferograms by using the measurements provided by a limited number of continuous GPS stations. These measurements are used to get an estimate of the long-term deformation signal, approximating a spatial ramp that is subsequently used to identify and filter out the orbital phase artifacts affecting the considered DInSAR interferograms. In this study, we apply this technique to analyze space geodetic data from a rather large (200 × 200 km) area around the San Andreas Fault (SAF) system in Southern California, USA (Fig. 1). This area is well suited for C-band radar interferometry, has a dense continuous GPS network (with some stations operating since early 1990 s) and has extensively been studied using space-geodetic methods (Johnson *et al.*, 1994; Bennett *et al.*, 1996; Fialko, 2006; Lundgren *et al.*, 2009). In this paper, we analyze a large set of ERS-1 and ERS-2 acquisitions spanning the 1992–2006 time interval and we generate mean LOS velocity maps and the corresponding deformation time series for each coherent pixel of the investigated area (i.e., for each pixel whose phase measurement is considered reliable). The derived time series are then compared to those provided by continuous GPS stations of the USGS/PBO networks (http://pasadena.wr.usgs.gov/scign/Analysis/) to identify secular and transient signals in surface velocities. Presented results considerably expand previously published LOS velocity data (Fialko, 2006; Lundgren *et al.*, 2009), both temporally (by adding 7 years of data from track 356) and spatially (by processing data from the adjacent track 127). In particular, the new data extend coverage to the central and northern sections of the San Jacinto fault (Fig. 1).

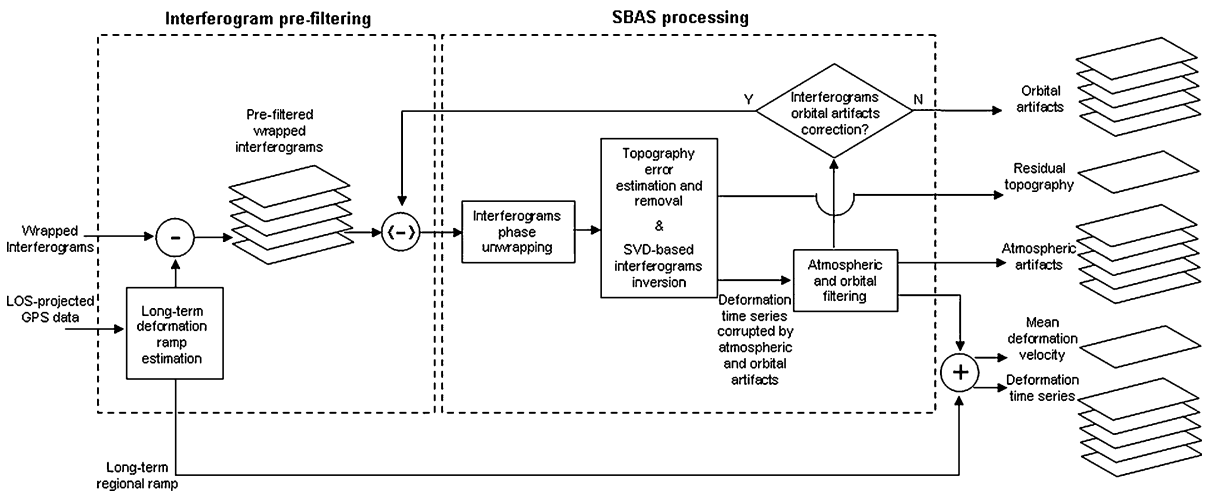

Figure 2
Block diagram of the exploited SBAS-DInSAR processing chain

Results presented in this paper highlight the necessity of a joint exploitation of SAR and GPS data in studies of interseismic deformation due to active faults in the Earth's crust. In particular, they provide detailed information about the temporal evolution and spatial distribution of the LOS velocities in the Southern SAF area. We present results of a comparison of the SBAS and LOS-projected GPS time series of the USGS/PBO network as well as mean LOS velocity fields derived using SBAS and stacking techniques. Our analysis shows a good agreement between these data sets and provides a quantitative assessment of the accuracy of the SBAS-DInSAR measurements in seismogenic areas.

The paper is organized as follows. First, we discuss the geological setting of the Southern SAF system. We then briefly describe the SBAS algorithm, highlighting the minor modifications required to make use of the GPS data. We then present and discuss the SBAS-DInSAR results obtained by jointly exploiting the radar and GPS measurements; in particular, we compare the retrieved DInSAR time series to the LOS-projected measurements of the available GPS network on selected sites and the mean deformation velocity map with that obtained

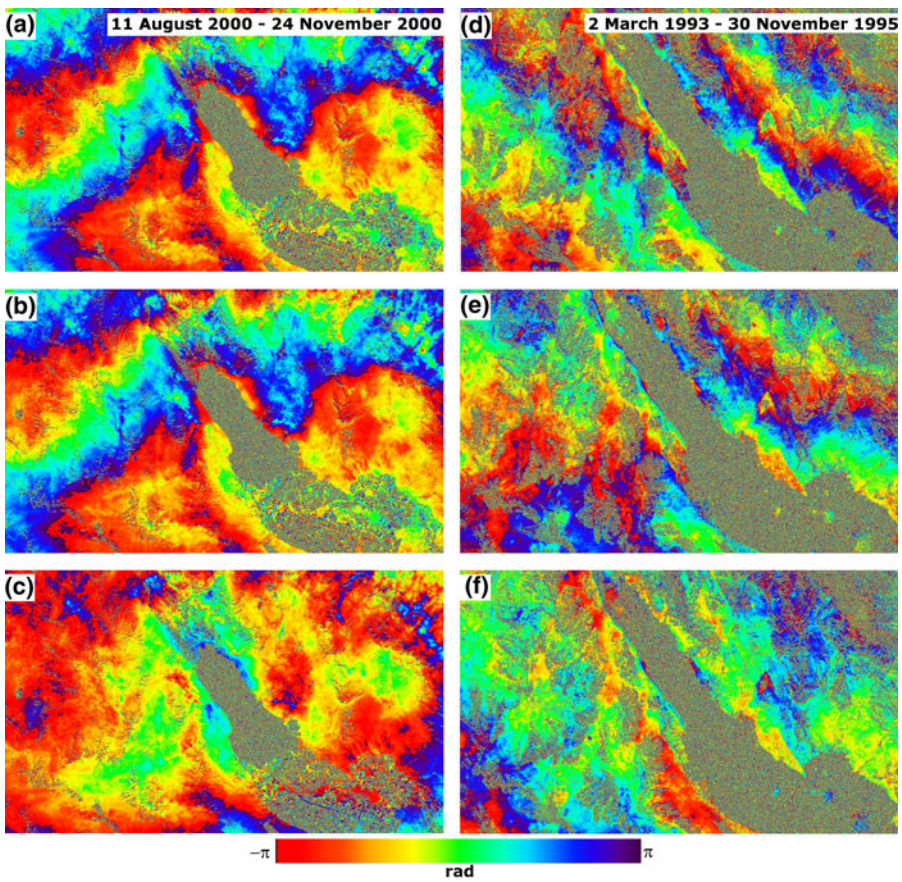

Figure 3
Impact of GPS driven pre-filtering versus orbital error correction for two selected ERS differential interferograms. **a** Original differential interferogram relevant to the 11 August 2000–24 November 2000 data pair; **b** differential interferogram compensated for the GPS-derived secular deformation pattern; **c** same as Fig. 3b, but also compensated for the orbital ramp. **d** Original differential interferogram relevant to the 2 March 1993–30 November 1995 data pair; **e** differential interferogram compensated for the GPS-derived secular deformation pattern; **f** same as Fig. 3e, but also compensated for the orbital ramp. Note that one full color cycle, say from *red to violet*, represents one interferometric phase fringe corresponding to a LOS-displacement of about 2.8 cm. We remark that the horizontal axis corresponds to the azimuth direction while the vertical one to the range

through the stacking technique and GPS. The last section is devoted to some conclusive remarks.

2. Tectonic Setting

Our study area is centered on the SAF system in Southern California (Fig. 1). This area is well suited for studies using DInSAR techniques. Arid climate and limited vegetation result in stability of reflective properties of the ground over time periods of the order of 10 years (Peltzer *et al.*, 2001; Lyons and Sandwell, 2003; Fialko, 2004, 2006). Extensive imaging of the area by the DInSAR-capable ERS-1/2 satellite missions of the European Space Agency, combined with a dense network of continuous GPS stations, gave rise to a geodetic dataset of excellent coverage and spatio-temporal resolution that can be exploited to characterize slow interseismic deformation due to the SAF system. The latter is a mature continental transform fault accommodating a significant fraction of the $\sim$0.05 m/yr relative motion between the North American and Pacific plates (e.g., Thatcher and Lisowski, 1987; DeMets *et al.*, 1990). Except for the 100-km long fault section between Parkfield and San Juan Batista that undergoes a steady creep, the SAF exhibits a stick–slip behavior and is capable of producing great earthquakes. The two most recent great earthquakes on the SAF have ruptured its central and northern sections in 1857 and 1906, respectively (see the inset of Fig. 1). The southernmost section of the SAF has not produced major earthquakes in historic time (over more than 300 years), as it is currently believed to be late in the interseismic phase of the earthquake cycle (Working Group on California Earthquake Probabilities, 1995; Weldon *et al.*, 2005; Fialko, 2006). Estimates of seismic hazard on the SAF as well as on other major faults in Southern California critically depend on the present-day strain rates and the degree of fault locking in the seismogenic crust (i.e., the presence and extent of fault creep). Both factors can in principle be evaluated with help of precise spatially dense measurements of surface deformation. In this paper, we quantitatively assess and validate DInSAR

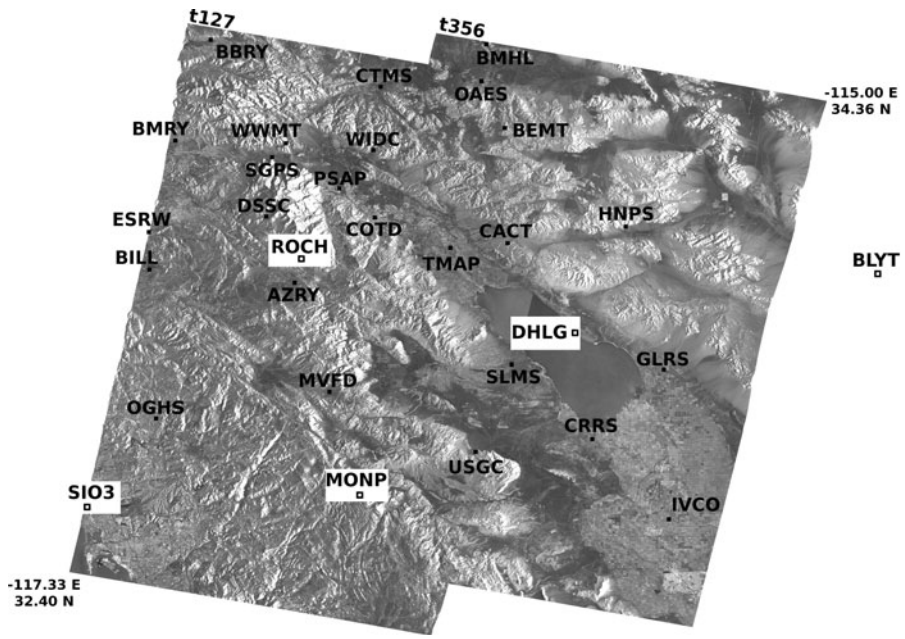

Figure 4
Mosaic of the multi-look SAR amplitude images of the investigated area for the SAR data belonging to 127 and 356 orbit tracks, that are presented in Fig. 5. The *black* and *white squares* mark the locations of the continuous GPS stations deployed in the area and belonging to the USGS/PBO network. Note that the *white ones* represent the five GPS stations selected to perform the estimate of the regional tectonic deformation rate

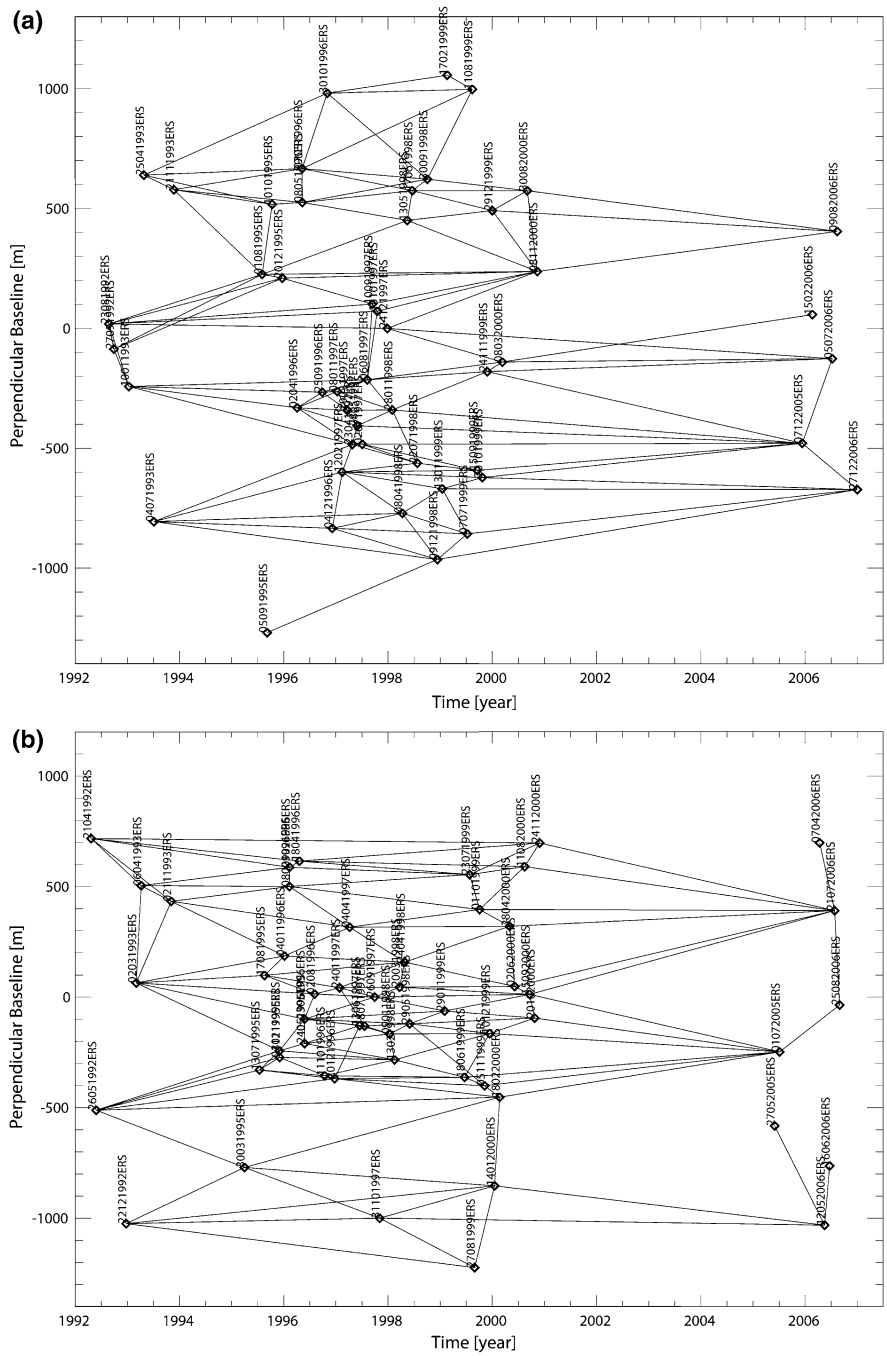

Figure 5
Interferometric data distribution on the temporal versus perpendicular baseline plane. The *diamonds* and *lines* represent the SAR acquisitions and data pairs, respectively. **a** SAR data distribution for track 127. **b** SAR data distribution for track 356

techniques commonly used for measuring subtle interseismic deformation and present analysis of DInSAR data from the Southern SAF collected between 1992 and 2006. The new results provide a much improved description of surface velocities; they can be used to constrain the geometry and kinematics of deep "roots" of faults comprising the Southern SAF system as well as to quantify the deformation

rates in the overlying nominally locked seismogenic crust.

3. SBAS-DInSAR Technique

The SBAS technique is a DInSAR algorithm that allows us to detect the Earth surface deformation and to analyze its temporal evolution by generating mean LOS velocity maps and time series of LOS displacements. In particular, this technique relies on the use of multiple master multi-look interferograms (Rosen *et al.*, 2000) generated via an appropriate selection of SAR data pairs characterized by small [less than a selected threshold, see Lanari *et al.*, (2007b)] spatial and temporal baselines. The key objective of this data selection is to mitigate the noise (decorrelation) effects, thus maximizing the number of temporally coherent pixels [for definition of temporal coherence, see Pepe and Lanari, (2006)]. Moreover, this baseline selection may imply that the data pairs used to produce the interferograms are arranged in few SBASs separated by large baselines. In the latter case, because there is no suitable interferogram that connects elements belonging to different subsets, they turn out to be independent of each other. Therefore, an underdetermined problem has to be solved, for instance by using a Least Squares minimization based on the singular value decomposition method (Berardino *et al.*, 2002).

In this work, we exploit the extended version of the SBAS technique (Casu *et al.*, 2008) that allows us to detect and analyze deformation phenomena with large spatial wavelength. This is done by exploiting relatively low resolution multi-look DInSAR interferograms computed from long SAR image strips, which are obtained by jointly focusing contiguous ERS raw data frames (belonging to the same satellite track). Following the generation of suitable interferograms, we average them on a grid of about 120 $\times$ 120 m and invert via the conventional SBAS technique (Berardino *et al.*, 2002) to retrieve the mean LOS velocity and the corresponding LOS displacement time series for each coherent pixel.

We point out that the SBAS inversion limits the impact of possible topographic artifacts present in the DEM used to compute the differential interferograms and improves the performance of the phase unwrapping procedure by making use of both the spatial and temporal variations in the radar phase among multiple interferograms (Pepe and Lanari, 2006). Moreover, the SBAS approach includes a filtering operation for the atmospheric phase components, based on the observation that the atmospheric phase signal is highly correlated in space but poorly in time (Goldstein, 1995; Ferretti *et al.*, 2000; Berardino *et al.*, 2002).

In addition to the atmospheric artifacts correction, the SBAS technique also includes a step for the detection and removal of orbital fringes (Lanari *et al.*, 2004b) that, as mentioned before, are well approximated by phase ramps. In particular, an estimate of these orbital patterns is performed by searching for the best-fit ramp to the retrieved time series signal component. This step leads to the generation of the required deformation time series. However, we remark that the orbital phase artifacts are particularly relevant in seismic areas, because it is not an easy task distinguishing between orbital artifacts and deformation signals that may mimic the orbital phase patterns. Accordingly, we propose to exploit the measurements from a limited number of continuous GPS stations in order to mitigate this problem. The rationale of the approach is quite simple and is focused on exploiting the GPS measurements in order to identify the long-wavelength interseismic signal; the GPS data are used to pre-filter the original differential interferograms representing the input of the SBAS processing. In particular, we first search for the best-fit ramp to the mean deformation velocity values of the selected GPS data that have been projected on the SAR sensor LOS in order to be consistent with the radar observations. Subsequently, we estimate and subtract the GPS-derived deformation ramp from each interferogram, by taking into account the time span of the considered interferometric pair. At this stage, the overall standard SBAS processing chain is applied to the pre-processed interferograms, including the orbital artifacts detection and removal step. However, in this case the filtering operation is more robust, because we have drastically mitigated the contribution of long term displacements that may be wrongly interpreted as being due to orbital errors.

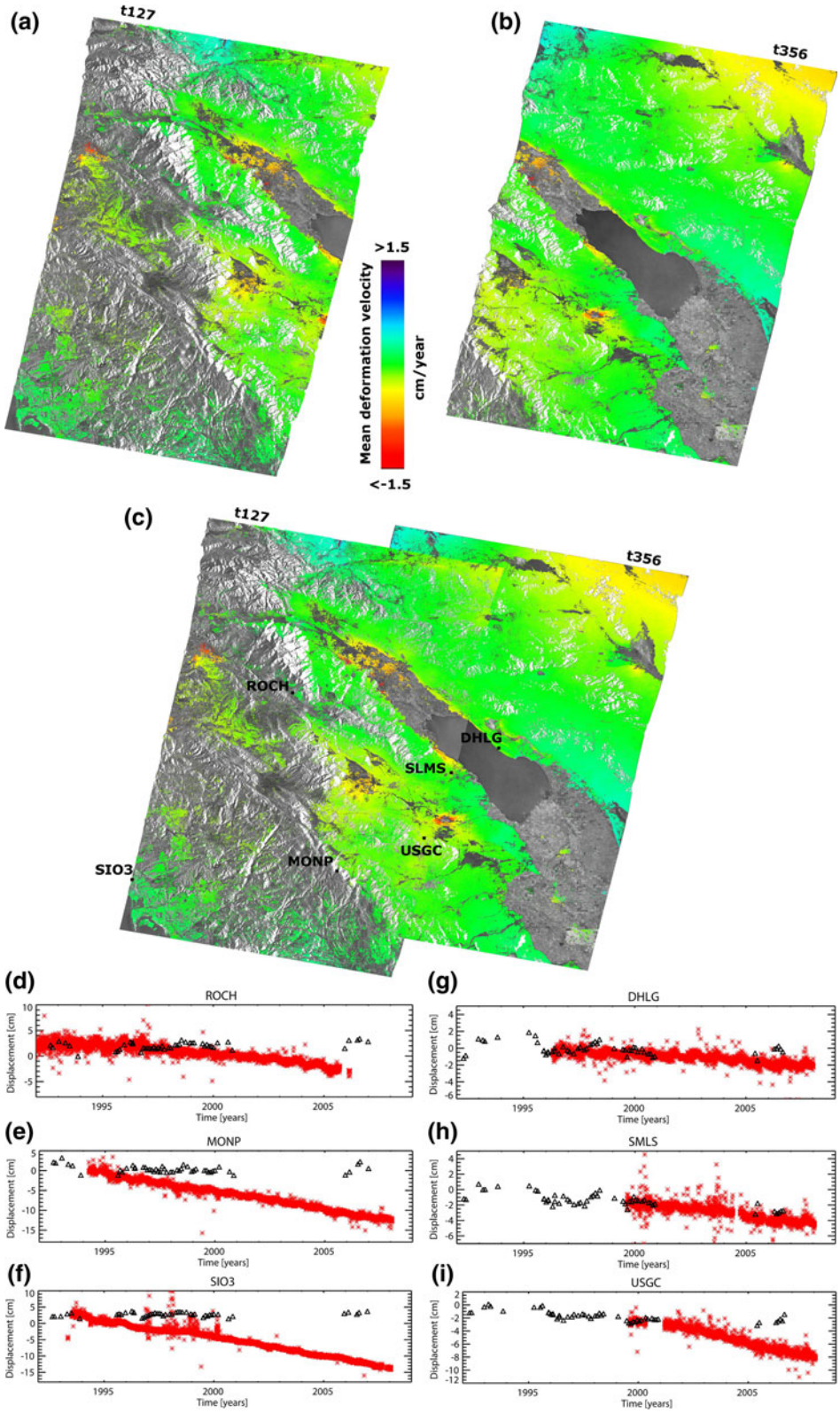
(a)
t127
(b)
t356
>1.5
Mean deformation velocity
cm/year
<-1.5
(c)
t127
t356
ROCH
DHLG
SLMS
USGC
MONP
SIO3
(d)
ROCH
(g)
DHLG
(e)
MONP
(h)
SMLS
(f)
SIO3
(i)
USGC
Displacement [cm]
Time [years]
1995
2000
2005

◀ Figure 6
SBAS-DInSAR results obtained by applying the conventional SBAS algorithm, where the orbital corrections were carried out without exploiting the available GPS measurements. **a**, **b** Mean deformation velocity maps for track 127 and track 356, geocoded and superimposed on the SAR images of the area. **c** Mosaic of the two velocity maps shown in Fig. 6a, b. **d–i** Comparison between the retrieved DInSAR measurements (*black triangles*) and the LOS-projected GPS time series (*red stars*), the latter obtained by projecting the displacement vector onto the radar LOS; data are relevant to the locations of the continuous GPS sites labeled in Fig. 6c as ROCH (**d**), MONP (**e**) and SIO3 (**f**) for track 127, and DHLG (**g**), SLMS (**h**) and USGC (**i**) for track 356

Note that at this stage we have available the orbital correction time series, i.e., the orbital ramps we estimate for each acquisition with respect to the first image of the time series. Accordingly, we may use them to correct the pre-filtered interferograms without introducing any inconsistency among interferograms. This operation may be relevant, particularly in low coherent areas, because it reduces, together with the GPS-derived correction, the phase gradient components, thus simplifying the phase unwrapping operation (Pepe and Lanari, 2006). We typically carry out just one iteration of this correction as a compromise between computing time and results accuracy.

Finally, in order to retrieve the actual surface motion across the fault, we add the GPS-retrieved long-term regional trend to the computed deformation time series. To summarize the rationale of the applied processing chain, we show its block diagram in Fig. 2.

The GPS measurements have been used to correct the DInSAR results before (e.g., Burgmann *et al.*, 2006; Gourmelen *et al.*, 2010). In this study, instead of using independent measurements to carry out a final correction of our deformation estimates, we exploit them to pre-filter the data in order to possibly improve the performances of the SBAS processing steps, particularly of the phase unwrapping operation.

We finally note that, although the proposed pre-filtering solution has a minor impact on the SBAS processing chain, it may play a fundamental role in the generation of the DInSAR results. To better clarify the impact of the GPS driven pre-filtering step vs. the orbital error correction, two examples are shown in Fig. 3, based on exploiting the SAR data presented in the following experimental results. In particular, we present in Fig. 3a the ERS differential interferogram corresponding to a short time interval 11 August 2000–24 November 2000 where a phase ramp is clearly visible. We remark that in this case the effect of the interseismic deformation retrieved through the GPS measurements is negligible due to the short time span and its removal has nearly no impact on the pre-filtered interferogram, see Fig. 3b. Accordingly, the detected phase ramp is fully due to orbital errors; the corrected interferogram is depicted in Fig. 3c. In contrast, Fig. 3d shows the interferogram covering a longer time interval, 2 March 1993–30 November 1995. In this case, again a phase ramp is visible but now, due to the significantly longer time span, it can be partially attributed to interseismic deformation. By compensating for this component, a significant correction is achieved (see Fig. 3e) and we may finally identify and compensate for the remaining orbital artifacts, as shown in Fig. 3f.

This simple example clearly highlights that in areas of active tectonic deformation a straightforward correction of orbital phase ramps may wrongly map ground motion into orbital errors. Accordingly, more advanced processing schemes are needed, particularly for deformation time series retrieval, as shown through the experiments presented in the next section.

4. SBAS-DInSAR Results

The SBAS-DInSAR processing chain summarized before and depicted in Fig. 2 has been applied to a set of ERS-1/2 SAR data acquired from two adjacent satellite tracks spanning the southern segment of the SAF system over the 1992–2006 time interval. Figure 4 shows the mosaic of the SAR amplitude images of the investigated area with the highlighted locations (black and white squares) of the continuous GPS stations belonging to the USGS/PBO network (http://pasadena.wr.usgs.gov/scign/Analysis/). The white squares denote five continuous GPS sites used to estimate the regional tectonic trend (note that the station named BLYT is slightly outside the radar swaths, located east of the studied area). These sites were chosen as they provide measurements since

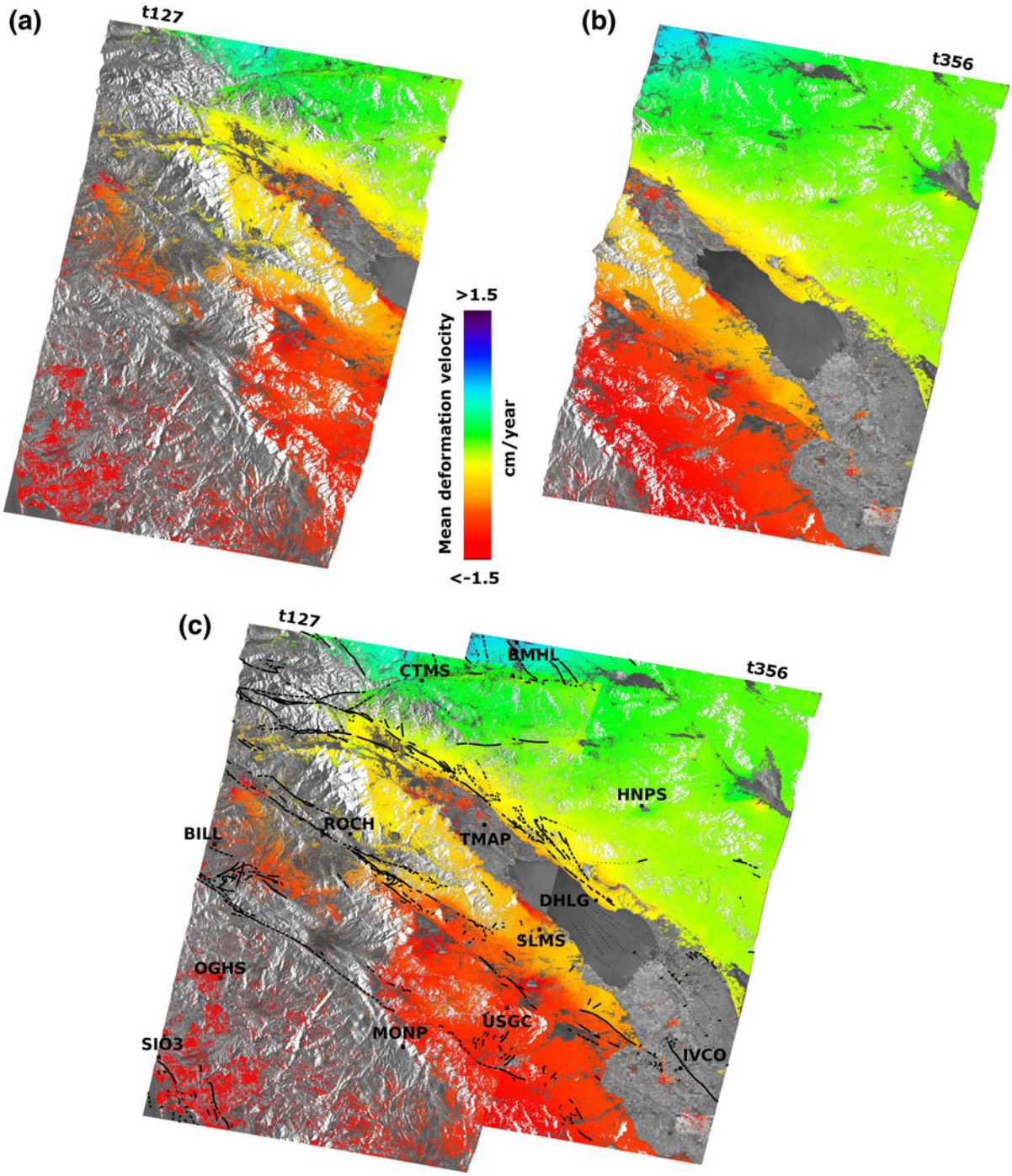

Figure 7
SBAS-DInSAR results obtained by applying the modified version of the SBAS algorithm, shown in Fig. 2, where the orbital corrections were carried out by exploiting the available GPS measurements. **a**–**b** Mean deformation velocity maps for track 127 (**a**) and track 356 (**b**). **c** Mosaic of the two velocity maps shown in Fig. 7a, b. The trace of the SAF system and the locations of the GPS sites relevant to the plots shown in Fig. 8 are indicated by the black lines and squares, respectively

1996 or earlier, thus ensuring at least 10 years of temporal overlap with the available SAR data.

We made use of 49 ERS acquisitions from the descending track 127 (frames: 2925–2943) to generate a set of 129 interferograms with a spatial resolution of about 120 × 120 m. We also used 53 ERS acquisitions from the descending track 356 (frames: 2925–2943) to generate 141 interferograms with the same spatial resolution. We chose the interferometric SAR pairs with a perpendicular baseline smaller than 450 m and a maximum Doppler Centroid separation of about 1100 Hz. This Doppler constraint is relevant since the ERS-2 SAR data acquired after year 2000, i.e., following the ERS-2 gyroscope failures (Miranda *et al.,* 2003), may give rise to large Doppler centroids. In our processing of SAR data we took advantage of precise satellite orbits provided by the Delft University and a 3-arcsec Digital Elevation Model (DEM) made available by the Shuttle Radar Topography Mission DEM (SRTM) (Rosen *et al*., 2001). In Fig. 5a, b a sketch of the exploited SAR images and of the implemented selection of DInSAR interferograms is shown for the data of the 127 and 356 tracks, respectively. All the SBAS results presented below (i.e., velocity maps and displacement time series) were computed with respect to a reference pixel chosen at the location of the BEMT continuous GPS station (see Fig. 4). The coregistered SAR images used to generate the interferograms were also used to compute the multi-look SAR amplitude images, as shown in Fig. 4.

To highlight the importance of a joint analysis of SAR and GPS data, we first present results obtained by applying the conventional SBAS algorithm, wherein the orbital corrections were carried out without exploiting the available GPS measurements.

Figure 6 shows the mean LOS velocity maps for tracks 127 and 356 (Fig. 6a and b, respectively), as well as the mosaic of the two maps (Fig. 6c), geocoded and superimposed on the SAR images of the area (see Fig. 4). Areas where the measurement accuracy is compromised by decorrelation are represented by the radar amplitude only. Note that results shown in Fig. 6 represent a time-averaged velocity of the Earth's surface in the satellite LOS. As one can see in Fig. 6, there exist some localized deformation anomalies, but the area is devoid of a long-wavelength deformation due to active faults. This is in contrast to the previously published results obtained using stacking (Fialko, 2006) and time series (Lundgren *et al*., 2009) techniques. SBAS-DInSAR results shown in Fig. 6 are wrong because a significant component of the long-wavelength deformation signal was misinterpreted as orbital ramps and filtered out; this clearly shows that a straightforward phase ramps filtering is inappropriate for tectonically active areas, such as Southern California. The impact of these errors is further demonstrated by a comparison between the retrieved LOS displacement time series at the locations of the continuous GPS sites and the GPS time series obtained by projecting the displacement vector onto the radar LOS (Fig. 6d–i).

Next, we present the results obtained by using the modified version of the SBAS-DInSAR algorithm described in Sect. 3 and sketched in Fig. 2. In particular, we show in Fig. 7 the mean LOS velocity maps for tracks 127 and 356 (Fig. 7a, b, respectively), as well as the mosaic of the two maps (Fig. 7c). In this case, one can clearly see a regional deformation pattern due to interseismic strain accumulation on major faults (in particular, the San Andreas and San Jacinto faults, see Fig. 1). In order to further investigate the inferred velocity field, we carried out an extensive comparison between the DInSAR-derived and the LOS-projected GPS time series. As previously, all displacements and velocities (SAR- and GPS-derived) were computed with respect to the reference BEMT site (Fig. 4). While our analysis involves measurements from all the GPS stations located in areas that are coherent within the DInSAR velocity maps, for illustration purposes we limited the comparison to 13 sites, as shown in Fig. 8. For each of the selected sites (whose locations are denoted by black squares in Fig. 7c) we compare the DInSAR results (black triangles) with the respective LOS-projected GPS displacements (red stars). The LOS projection of the GPS data used local radar incidence angles. Inspection of Fig. 8 reveals a generally good agreement between the LOS displacement time series derived from DInSAR and GPS data. The overall agreement is perhaps not surprising for stations ROCH, MONP, DHLG and SIO3 that were used to estimate the

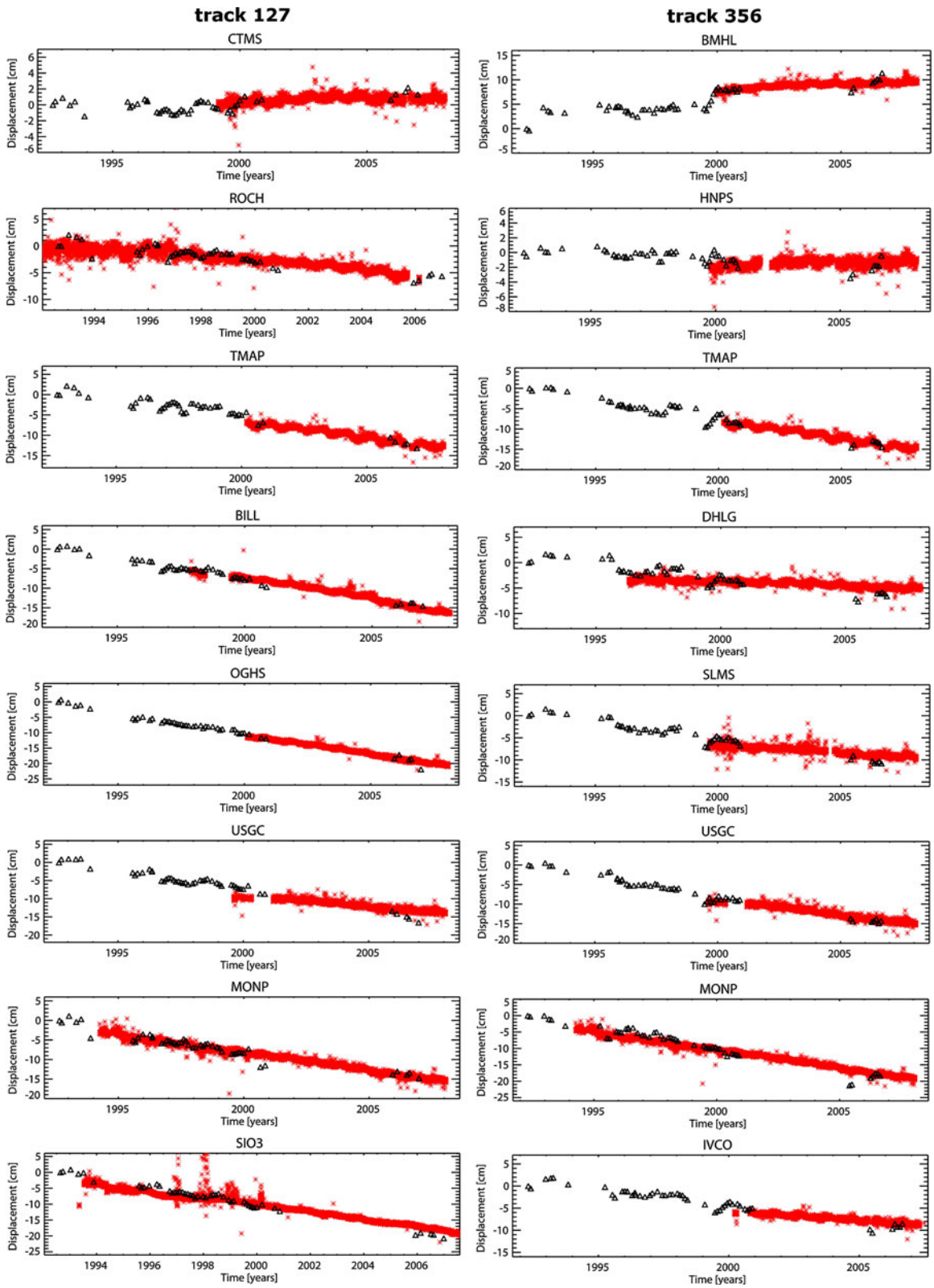
track 127
track 356
CTMS
BMHL
ROCH
HNPS
TMAP
TMAP
BILL
DHLG
OGHS
SLMS
USGC
USGC
MONP
MONP
SIO3
IVCO
Displacement [cm]
Time [years]

◀ Figure 8
Comparison between the retrieved DInSAR deformation measurements (*black triangles*) and the LOS-projected GPS time series (*red stars*) for the continuous GPS sites identified in Fig. 7c; DInSAR time series versus GPS measurements for the sites of track 127 are shown on left side, while those for the sites of track 356 are on the right

orbital ramps, as discussed in Sect. 3. Importantly, a rather good agreement is also observed for other stations (Fig. 8), although minor discrepancies persist in some cases. We evaluated the accuracy of the DInSAR results by computing the standard deviation of the differences between the DInSAR and the LOS-projected GPS displacements for all the sites identified in Fig. 4 by the black and white squares (except for the BLYT station where no DInSAR measurements were available); the obtained results are summarized in Tables 1 and 2 for data from tracks 127 and 356, respectively. Based on these measurements, we computed the average standard deviation (σ) value representative of the differences between the DInSAR and LOS-projected GPS data; for both tracks we obtained $\sigma \approx 1.2$ cm. This result is in good agreement with that previously reported by Casu *et al.* (2006) and Tizzani *et al.* (2007). It clearly confirms the need to account for long-wavelength deformation in the SBAS-DInSAR analysis, using auxiliary geodetic data to effectively filter out orbital artifacts. In order to further clarify the impact of the carried out correction of the DInSAR results, we also present in Tables 3 and 4 the standard deviations of the differences between the LOS-projected GPS displacements (also in this case for all the sites identified in Fig. 4 by the black and white squares) and the DInSAR time series without any correction (left column) and with the correction of the orbital artifacts only (right column) for data from tracks 127 and 356, respectively. By considering Tables 3 and 4 it is evident that the orbital artifacts correction can be very relevant as for the case of track 127 for which the impact of the correction of the DInSAR time series exceeds 1 cm on average; this exceeds by a factor of two the effect of filtering of atmospheric artifacts (Tables 1 and 2).

To provide a visual interpretation of the impact of the orbital artifacts, in Fig. 9 we present the DInSAR

Table 1

Results of the comparison between LOS-projected GPS measurements and DInSAR deformation time series relevant to track 127

GPS stations	Standard deviation of the difference between LOS-projected GPS and DInSAR measurements (cm)
AZRY	1.2
BBRY	1.9
BILL	0.9
BMRY	1.3
CACT	0.8
COTD	1.8
CTMS	0.8
DSSC	1.4
ESRW	0.6
MONP	1.0
MVFD	1.3
OAES	1.0
OGHS	1.1
PSAP	1.5
ROCH	1.1
SGPS	0.8
SIO3	2.4
SLMS	1.9
TMAP	0.7
USGC	2.4
WIDC	1.3
WWMT	0.2
Average value	1.2

Table 2

Results of the comparison between LOS-projected GPS measurements and DInSAR deformation time series relevant to track 356

GPS stations	Standard deviation of the difference between LOS-projected GPS and DInSAR measurements (cm)
BMHL	0.8
CACT	0.4
CRRS	1.1
DHLG	1.5
GLRS	1.2
HNPS	1.3
IVCO	1.5
MONP	1.7
OAES	1.6
SLMS	1.5
TMAP	0.7
USGC	0.9
Average value	1.2

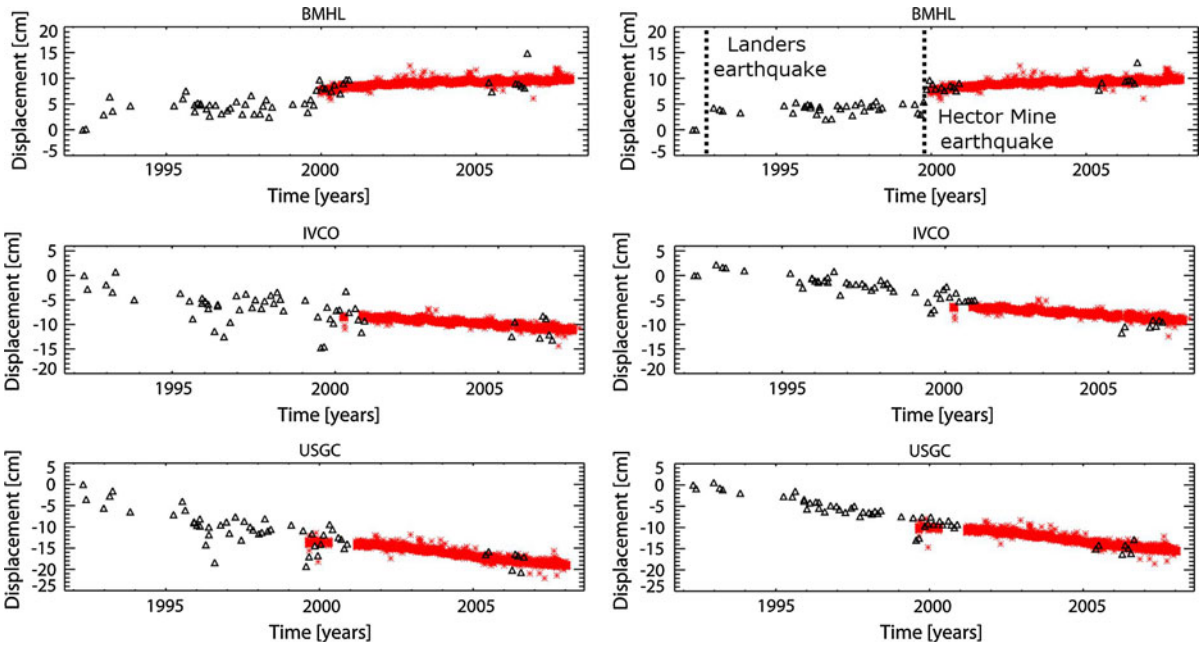

Figure 9
Comparison between the retrieved DInSAR deformation time series for data belonging to track 356 (*black triangles*) and the LOS-projected GPS measurements (*red stars*) at the locations of the continuous GPS sites labeled as BMHL, IVCO and USGC (Fig. 4). *Left*: the DInSAR time series are computed without orbital artifact correction; *right*: the DInSAR time series are computed with the orbital ramp correction. Note that the *vertical dashed lines* identify the dates of the Landers and Hector Mine earthquakes

time series for track 356 without (left column) and with (right column) orbital correction for three selected GPS sites labeled as BMHL, IVCO and USGC. The relevance of this correction is evident, particularly for the BMHL site, where it allows us to clearly identify, even without any atmospheric filtering, the effect of the Hector Mine earthquake (16 October 1999) and, particularly, of the Landers earthquake (28 June 1992). Therefore, although the impact of our correction for track 356 is not very prominent on average (a few mm, see Table 4), it may play an important role for the investigation of specific seismic events.

For sake of completeness, we also report similar results for track 127, see Fig. 10, where we selected the sites BILL, OGHS and USGC. The success of the correction for BILL and OGHS is evident, as already expected from Table 3. We also report the less favorable case of the USGC site, where our analysis reveals that the computed standard deviation exceeds 2 cm. This result may suggest the need for higher-order corrections for the regional tectonic deformation, for instance, using interpolated velocities from the entire GPS network.

Finally, we also performed a comparison between the mean LOS velocity field obtained using the SBAS algorithm with the results of optimized stacking procedure in which each SAR acquisition is assigned a weight according to the estimated atmospheric noise contribution (Fialko, 2004). Raw SAR data were processed using JPL/Caltech ROI_PAC software with phase unwrapping using the SNAPHU algorithm (Chen and Zebker, 2002). Figure 11b shows a comparison of the mean LOS velocities from the ERS track 356 across the SAF zone. The profile, highlighted in Fig. 11a, corresponds to that used by Fialko (2006). There is an overall agreement between the LOS velocities obtained using the different DInSAR processing algorithms. The accuracy of both methods is further validated by the good agreement

with the mean GPS velocities projected onto the satellite LOS, thus confirming the expected accuracy of about 1–2 mm/year.

We finally remark that, although the presented results are focused on interseismic deformation, the analysis of the computed time series in principle allows one to accurately measure also coseismic displacements. Compared to the analysis of conventional interferograms spanning over the earthquake date, advantages offered by the SBAS technique include removal of the phase artifacts (e.g., due to orbital errors and atmospheric noise) and no need for phase unwrapping. We illustrate this approach by measuring deformation due to the 1992 Landers earthquake using the time series from track 356. The inferred coseismic range changes are shown in Fig. 12a. The earthquake signal is clearly visible in the northwest corner of the image. For comparison, we also present three conventional interferogram spanning the time intervals 26 May 1992–17 November 1992, 26 May 1992–22 December 1992 and 21 April 1992–6 April 1993, respectively (Fig. 12e–g). Figure 12b–d shows the time series for three selected positions within the radar image (see Fig. 12a) with the interseismic trend removed. Coseismic displacements shown in Fig. 12a represents a jump in the inferred LOS displacements between the SAR acquisitions bracketing the earthquake date. Although the Landers event is not optimal for recovery of coseismic deformation as there are few pre-earthquake acquisitions (so that the preseismic rates are not resolved), an overall agreement between the displacement fields shown in Fig. 12a and those in Fig. 12e–g is encouraging. In particular, as expected, the coseismic

Table 3

Results of the comparison between GPS measurements and DInSAR deformation time series relevant to track 127; for the latter we considered the unfiltered results (left column) and those corrected for the orbital artifacts only (right column)

GPS stations	Standard deviation of the difference between LOS-projected GPS and unfiltered DInSAR measurements (cm)	Standard deviation of the difference between LOS-projected GPS and DInSAR measurements corrected for the orbital artifacts only (cm)
AZRY	3.0	1.4
BBRY	4.5	3.0
BILL	3.4	1.3
BMRY	4.5	1.6
CACT	0.9	0.8
COTD	1.2	2.4
CTMS	2.3	1.0
DSSC	3.1	1.6
ESRW	3.0	1.1
MONP	2.5	2.1
MVFD	2.9	1.5
OAES	1.7	1.0
OGHS	5.1	1.0
PSAP	1.9	1.9
ROCH	2.7	1.5
SGPS	2.8	0.8
SIO3	3.8	2.6
SLMS	2.9	3.1
TMAP	1.9	2.1
USGC	3.8	3.0
WIDC	1.7	1.6
WWMT	2.3	0.3
Average value	2.8	1.7

Table 4

Results of the comparison between GPS measurements and DInSAR deformation time series relevant to track 356; for the latter we considered the unfiltered results (left column) and those corrected for the orbital artifacts only (right column)

GPS stations	Standard deviation of the difference between LOS-projected GPS and unfiltered DInSAR measurements (cm)	Standard deviation of the difference between LOS-projected GPS and DInSAR measurements corrected for the orbital artifacts only (cm)
BMHL	1.7	1.1
CACT	0.8	0.6
CRRS	2.3	1.9
DHLG	2.4	2.2
GLRS	2.0	1.6
HNPS	1.2	1.5
IVCO	2.9	1.8
MONP	2.4	2.7
OAES	1.7	1.6
SLMS	2.1	2.2
TMAP	1.2	1.3
USGC	2.3	1.6
Average value	1.9	1.7

displacement map obtained from the time series analysis (Fig. 12a) is less affected by artifacts such as atmospheric noise (cf. Fig. 12e–g) due to the mentioned filtering steps implemented through the SBAS processing. We note that the inferred time series (Fig. 12b–d) appear to have an overall pattern similar to the post-seismic GPS data (e.g., FIALKO, 2004; Fig. 8), although relatively sparse SAR acquisitions following the Landers earthquake do not allow one to determine whether the range changes between 1992 and 1993 evident in Fig. 12b–d represent primarily coseismic deformation or also include a rapid post-seismic response. The nature of a rather broad anomaly in the LOS displacements at the eastern side of the radar image is not clear and might be due to residual orbital or propagation errors. Further investigations are required to validate coseismic applications of the SBAS time series analysis.

5. Conclusions

We have investigated the capability of the SBAS-DInSAR technique to measure secular deformation in active seismogenic areas. In particular, the focus of this work is on a 200 × 200 km area around the Coachella Valley section of the SAF in Southern California (USA). The analysis is carried out by exploiting the data acquired by the ERS-1/2 sensors from two adjacent tracks (127 and 356) during the 1992–2006 time interval. Results presented in this paper provide a clear picture of the ongoing interseismic deformation due to the Southern SAF system, extending the data coverage compared to previous analyses both in space (by adding track 127) and in time (by including data from the 2000–2006 epoch).

To achieve the presented results, we show the relevance of exploiting external measurements from

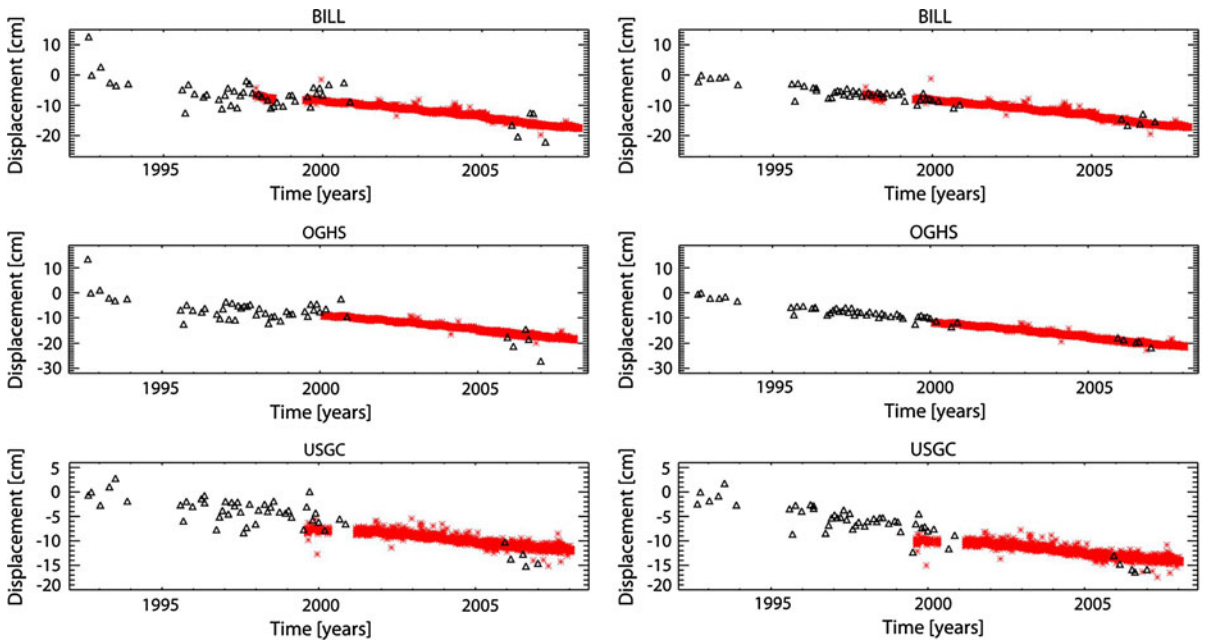

Figure 10
Comparison between the retrieved DInSAR deformation time series for data belonging to track 127 (*black triangles*) and the LOS-projected GPS measurements (*red stars*) at the locations of the continuous GPS sites labeled as BILL, OGHS and USGC (Fig. 4). *Left*: the DInSAR time series are computed without orbital artifact correction; *right*: the DInSAR time series are computed with the orbital ramp correction

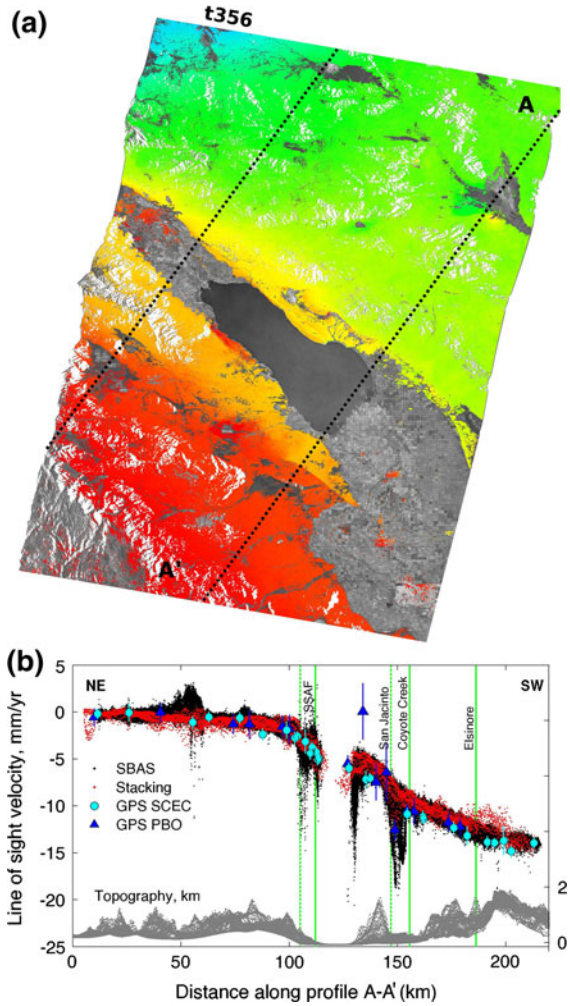

Figure 11
a Mean deformation velocity map for track 356 (same as for Fig. 7b) where the *dashed strip* outlines a profile from which the DInSAR and GPS data are extracted for the comparison shown in Fig. 11b. **b** LOS velocities as inferred from the modified SBAS analysis (*black dots*) and optimized stacking (*red dots*). *Color symbols* represent LOS-projected GPS data. Campaign GPS data from the SCEC velocity model are denoted by *circles* and continuous data from the PBO network by *triangles*. *Vertical green lines* denote the location of active faults (see FIALKO (2006) for details)

continuous GPS stations in order to discriminate the interferometric phase signal components due to long-wavelength deformation, caused by interseismic strain accumulation, from that caused by orbital artifacts. In particular, we propose a simple solution, with a minimum impact on the SBAS procedure that is based on pre-filtering of the DInSAR interferograms by using the available measurements of a limited set of continuous GPS stations. In particular, this pre-filtering step allows us to successfully compensate, within the SBAS processing, for orbital artifacts because it drastically mitigates the presence of long-wavelength interseismic displacements that may be wrongly interpreted and filtered out as orbital phase errors.

By comparing these results with those available through the local USGS/PBO continuous GPS network, we show that the orbital phase correction is, at least for one of the two time series, even more relevant than the atmospheric phase filtering. We also show the achieved accuracy of the finally retrieved deformation time series is consistent with that obtained through previous SBAS product validation analyses focused on different deformation scenarios. Moreover, there is also a very good agreement between the estimated mean deformation velocity and that computed using optimized stacking techniques.

We finally remark that the presented work is focused on a specific case study but it can be easily extended to other seismic areas. In this context, the full exploitation of the available huge archives of C-band SAR data, which are largely unused, can be of great importance for carrying out new analysis of occurred seismic events as well as for quantifying subtle interseismic strain accumulation in tectonically active areas. In these scenarios, the spatial distribution and density of the exploited continuous GPS stations can play a significant role. Indeed, a GPS network adequately "covering" the whole study area, with measurements that significantly overlap with the interval of the DInSAR time series, is clearly needed. An extended investigation of the trade-off between the GPS distribution/density and the accuracy of the retrieved DInSAR results is outside the scope of this work, but it is certainly worth for future analysis in order to assess the requirements and

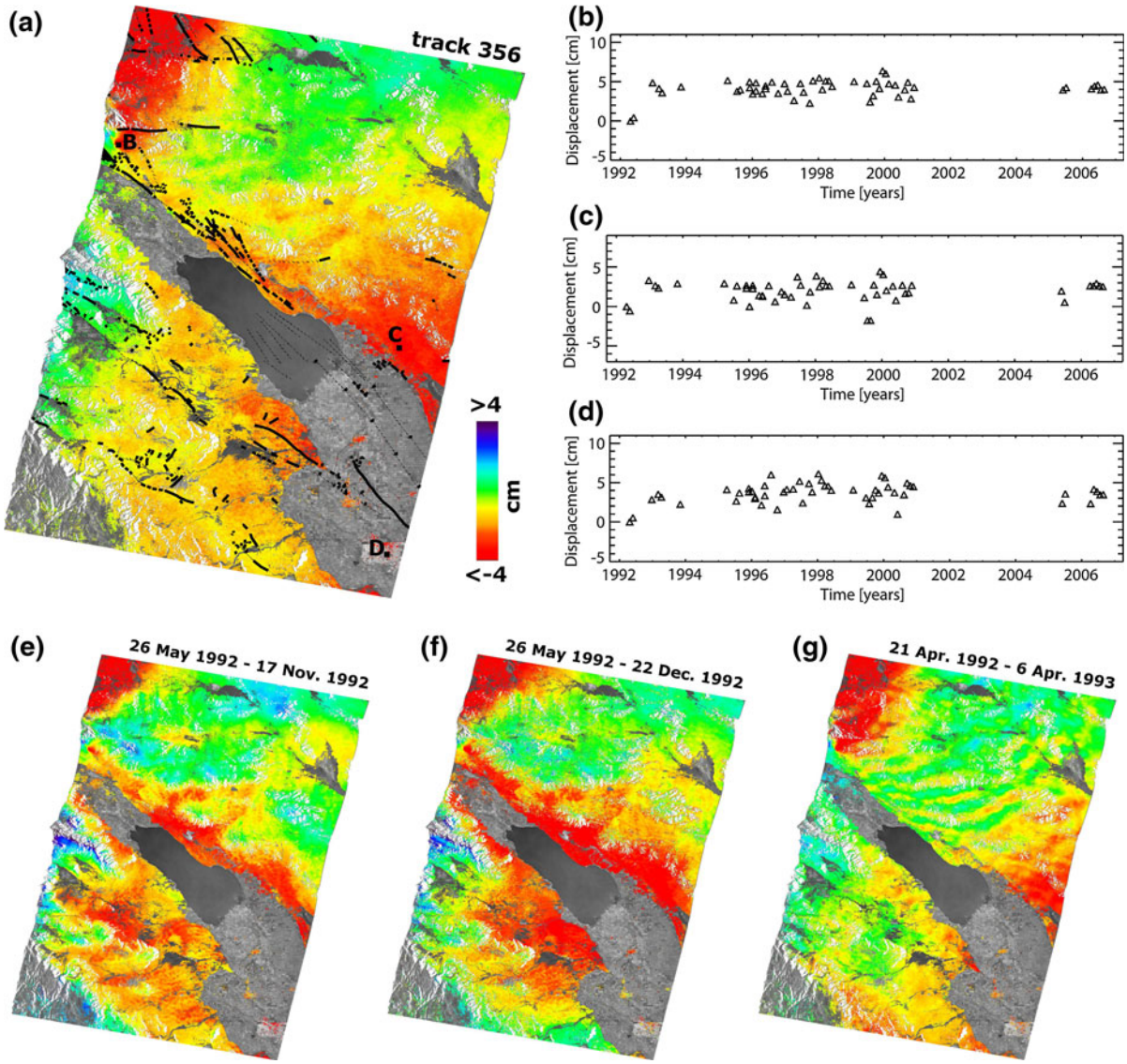

Figure 12

a Deformation map due to the Landers earthquake (28 June 1992) computed from time series of track 356; the trace of the SAF system is identified via black lines. **b–d** Detrended time series computed without atmospheric filtering at the locations referred to as *B*, *C* and *D* in Fig. 12a. **e–g** Unwrapped interferograms relevant to the 26 May 1992–17 November 1992 (**e**), 26 May 1992–22 December 1992 (**f**) and 21 April 1992–6 April 1993 (**g**) time intervals. Note that the exploited ERS image acquired on 17 November 1992 is not included in the generated DInSAR time series because it was available only subsequently

performance of the proposed approach that jointly exploits GPS and DInSAR measurements.

Acknowledgments

This work has partially been supported by ASI, the Italian DPC, NASA (NNX09AD23G) and USGS (G09AP00025). ERS SAR data used in this study are copyright of ESA, acquired via the WInSAR Consortium (http://winsar.unavco.org). We thank the Technical University of Delft, The Netherlands, for precise ERS-1/2 orbits. SRTM digital elevation data were produced by NASA and distributed by USGS. Finally, we thank S. Guarino, F. Parisi and M.C. Rasulo for their technical support.

References

Amelung, F., Galloway, D.L., Bell, J.W., Zebker, H.A., and Laczniak, R.J. (1999), *Sensing the ups and downs of Las Vegas: InSAR reveals structural control of land subsidence and aquifer-system deformation*, Geology, *27*, 483–486.

Bennett, R. A., Rodi, W. and Reilinger, R. E. (1996), *Global positioning system constraints on fault slip rates in southern California and northern Baja, Mexico*, J Geophys Res *101*, 21943–21960.

Berardino, P., Fornaro, G., Lanari, R. and Sansosti, E. (2002), *A new algorithm for surface deformation monitoring based on small baseline differential SAR interferograms*, IEEE Trans. Geosci Remote Sens *40*, 2375–2383.

Biggs, J., Wright, T., Lu, Z., and Parsons, B. (2007), *Multi-interferogram method for measuring interseismic deformation: Denali fault, Alaska*, Geophys J Int *170*, 1165–1179.

Burgmann, R., Hilley, G., Ferretti, A. and Novali F. (2006), *Resolving vertical tectonics in the San Francisco Bay Area from permanent scatterer InSAR and GPS analysis*, Geology *34*, 221–224.

Casu, F., Manzo, M., and Lanari, R. (2006), *A quantitative assessment of the SBAS algorithm performance for surface deformation retrieval from DInSAR data*, Remote Sens Environ *102*(3–4), 195–210, doi:10.1016/j.rse.2006.01.023.

Casu, F., Manzo, M., Pepe, A., and Lanari, R. (2008), *SBAS-DInSAR Analysis of Very Extended Areas: First Results on a 60,000 km2 Test Site*, IEEE Geosci Remote Sens Lett *5* 3, doi: 10.1109/LGRS.2008.916199.

Chen, C. W., and Zebker, H. A. (2002), *Phase unwrapping for large SAR interferograms: Statistical segmentation and generalized network models*, IEEE Transactions on Geoscience and Remote Sensing *40*, pp. 1709–1719.

DeMets, C., Gordon, R. G., Argus, D. F., and Stein, S. (1990), *Current plate motions*, Geophys. J Int *101*, 425–478.

Ferretti, A., Prati, C., and Rocca, F.(2000), *Non-linear subsidence rate estimation using permanent scatterers in differential SAR interferometry*, IEEE Transaction on Geoscience and Remote Sensing *38*, 5.

Fialko, Y., Simons, M., and Agnew, D. (2001), *The complete (3-D) surface displacement field in the epicentral area of the 1999 Mw7.1 Hector Mine earthquake, California, from space geodetic observations*, Geophys Res Lett *28*, 3063–3066.

Fialko, Y. (2004), *Evidence of fluid-filled upper crust from observations of post-seismic deformation due to the 1992 Mw7.3 Landers earthquake*, J Geophys Res, *109*, B08401, doi:10.1029/2003JB002985.

Fialko, Y. (2006), *Interseismic strain accumulation and the earthquake potential on the southern San Andreas fault system*, Nature, *441*, doi:10.1038/nature04797, 968–971.

Gabriel, A. K., Goldstein, R. M., and Zebker, H. A. (1989), *Mapping small elevation changes over large areas: Differential interferometry,* J Geophys Res *94*, 9183–9191.

Goldstein, R. M. (1995), *Atmospheric limitations to repeat-track radar interferometry,* Geophys Res Lett *22*, 2517−2520.

Gourmelen, N., Amelung F., and Lanari R. (2010), *InSAR–GPS Integration: inter-seismic strain accumulation across the hunter mountain fault in the eastern California shear zone*, J Geophys Res doi:10.1029/2009JB007064, in press.

Hooper, A., Zebker, H., Segall, P., and Kampes, B. (2004), *A new method for measuring deformation on volcanoes and other natural terrains using InSAR persistent scatterers*, Geophys Res Lett *31*, L23611, doi:10.1029/2004GL021737.

Hooper, A. (2008), *A multi-temporal InSAR method incorporating both persistent scatterer and small baseline approaches*, Geophys Res Lett *35* L16302, doi:10.1029/2008GL034654.

Johnson, H. O., Agnew, D. C., and Wyatt, F. K. (1994), *Present-day crustal deformation in southern California*, J Geophys Res *99*, 23951–23974.

Lanari, R., Mora, O., Manunta, M., Mallorquí, J. J., Berardino, P., and Sansosti, E. (2004a), *A small baseline approach for investigating deformations on full resolution differential SAR interferograms*, IEEE Trans Geosci Remote Sens *42*, 7.

Lanari, R., Lundgren, P., Manzo, M., and Casu F. (2004b), *Satellite radar interferometry time series analysis of surface deformation for Los Angeles, California*, Geophys Res Lett *31*, L23613, doi:10.1029/2004GL021294.

Lanari, R., Casu, F., Manzo, M., and Lundgren, P. (2007a), *Application of the SBAS-DInSAR technique to fault creep: a case study of the Hayward fault, California*, Remote Sens Environ J *109*, 1, 20–28, doi:10.1016/j.rse.2006.12.003.

Lanari, R., Casu, F., Manzo, M., Zeni, G., Berardino, P., Manunta, M., and Pepe, A. (2007b), *An Overview of the Small BAseline Subset Algorithm: a DInSAR Technique for Surface Deformation Analysis*, Pure Appl Geophys (PAGEOPH), *164*, 4, 637–661, doi:10.1007/s00024-007-0192-9.

Lundgren, P. E., Hetland, A., Liu, Z. and Fielding, E. J. (2009), *Southern San Andreas-San Jacinto fault system slip rates estimated from earthquake cycle models constrained by GPS and interferometric synthetic aperture radar observations*, J Geophys Res *114*, B02403, doi:10.1029/2008JB005,996.

Lyons, S. and Sandwell, D. (2003), *Fault creep along the southern San Andreas from interferometric synthetic aperture radar, permanent scatterers, and stacking*, J Geophys Res *108*, doi: 10:1029/2002JB001831.

Manzo, M., Ricciardi, G. P., Casu, F., Ventura, G., Zeni, G., Borgström, S., Berardino, P., Del Gaudio, C., and Lanari, R. (2006), *Surface deformation analysis in the Ischia island (Italy) based on spaceborne radar interferometry*, J Volcanol Geotherm Res *151*, 399–416, doi:10.1016/j.jvolgeores.2005.09.010.

Massonnet, D., Rossi, M., Carmona, C., Adragna, F., Peltzer, G., Feigl, K., and Rabaute, T. (1993), *The displacement field of the Landers earthquake mapped by radar interferometry*, Nature, *364*, 138–142.

Massonnet, D., Briole, P., and Arnaud, A. (1995), *Deflation of Mount Etna monitored by spaceborne radar interferometry*, Nature, *375*, 567–570.

Miranda, N., Rosich, B., Santella, C., and Grion, M. (2003), Review of the impact of ERS-2 piloting modes on the SAR Doppler stability, Proceedings Fringe '03, 1-5 December 2003, Frascati, Italy.

Mora, O., Mallorqui, J. J., and Broquetas, A. (2003), *Linear and nonlinear terrain deformation maps from a reduced set of interferometric SAR images*, IEEE Trans Geosci Remote Sens *41*, 2243–2253.

Neri, M., Casu, F., Acocella, V., Solaro, G., Pepe, S., Berardino, P., Sansosti, E., Caltabiano, T., and Lundgren, P. (2009), *Deformation and eruptions at Mt. Etna (Italy): A lesson from 15 years of observations*, Geophy Res Lett *36*, doi:10.1029/2008GL036151.

PELTZER, G., and ROSEN, P.A. (1995), *Surface displacement of the 17 May 1993 Eureka Valley earhtquake observed by SAR interferometry*, Science *268*, 1333–1336.

PELTZER, G., CRAMPE, F., HENSLEY, S., and ROSEN, P. (2001), *Transient strain accumulation and fault interaction in the Eastern California shear zone*, Geology *29*, 975–978.

PEPE, A., and LANARI, R. (2006), *On the extension of the minimum cost flow algorithm for phase unwrapping of multitemporal differential SAR interferograms*, IEEE Trans Geosci Remote Sens *44*, 9, 2374–2383.

PRATI, C., FERRETTI, A., and PERISSIN, D. (2010), *Recent advances on surface ground deformation measurement by means of repeated space-borne SAR observations*, J Geodynamics *49*, 161–170.

RIGNOT, E. (1998), *Fast recession of a west Antarctic glacier*, Science, *281*, 549–551.

ROSEN, P. A., HENSLEY, S., JOUGHIN, I. R., LI, F. K., MADSEN, S. N., RODRIGUEZ, E., *et al.* (2000). Synthetic aperture radar interferometry, IEEE Proceedings, 88, 333–376.

ROSEN, P. A., HENSLEY, S., GURROLA, E., ROGEZ, F., CHAN, S., and MARTIN, J. (2001), *SRTM C-band topographic data quality assessment and calibration activities*, Proc. of IGARSS'01, 739–741.

THATCHER, W., and LISOWSKI, M. (1987), *Long-term seismic potential of the San-Andreas fault southeast of San-Francisco*, California J Geophys Res *92*, 4771–4784.

TIZZANI, P., BERARDINO, P., CASU, F., EUILLADES, P., MANZO, M., RICCIARDI, G. P., ZENI, G., and LANARI, R. (2007), *Surface deformation of Long Valley caldera and Mono Basin, California, investigated with the SBAS-InSAR approach*, Remote Sens Environ J *108*, 277–289, doi:10.1016/j.rse.2006.11.015.

WELDON, R.J., FUMAL T. E., BIASI G. P., SCHARER K. M. (2005), *Geophysics: past and future earthquakes on the San Andreas fault*, Science, *308*, 5724, 966–967.

WERNER, C., WEGMÜLLER, U., STROZZI, T. and WIESMANN, A. (2003), Interferometric point target analysis for deformation mapping, Proc. IGARSS'03, Toulouse (France), 4362–4364.

WORKING GROUP ON CALIFORNIA EARTHQUAKE PROBABILITIES (1995), *Seismic hazards in southern California: Probable earthquakes, 1994–2024*. Bull Seism Soc Am *85*, 379–439.

WRIGHT, T. J., PARSONS, B., ENGLAND, P. C., and FIELDING, E. J. (2004), *InSAR observations of low slip rates on the major faults of western Tibet*, Science *305*, 236–239.

(Received July 13, 2010, revised February 9, 2011, accepted April 11, 2011)